J. Fluid Mech. (2014), *vol.* 757, *pp.* 57–81.
doi:10.1017/jfm.2014.479

Flow and heat transfer in convectively unstable turbulent channel flow with solid-wall heat conduction

Anirban Garai[1,‡], **Jan Kleissl**[1,†] **and Sutanu Sarkar**[1]

[1]Department of Mechanical and Aerospace Engineering, University of California, San Diego, CA 92093, USA

(Received 15 October 2013; revised 3 August 2014; accepted 15 August 2014; first published online 19 September 2014)

Most turbulent coherent structures in a convectively unstable atmospheric boundary layer are caused by or manifested in ascending warm fluid and descending cold fluids. These structures not only cause ramps in the air temperature timeseries, but also imprint on the underlying solid surface as surface temperature fluctuations. The coupled flow and heat transport mechanism was examined through direct numerical simulation (DNS) of a channel flow allowing for realistic solid–fluid thermal coupling. The thermal activity ratio (*TAR*; the ratio of thermal inertias of fluid and solid), and the thickness of the solid domain were found to affect the solid–fluid interfacial temperature variations. The solid–fluid interface with large (small) thermal activity ration behaves as an isoflux (isothermal) boundary. For the range of parameters considered here (Grashof number, $Gr = 3 \times 10^5$–325×10^5; $TAR = 0.01$–1; solid thickness normalized by heat penetration depth $= 0.1$–10), the solid thermal properties and thickness influence the fluid temperature only in the viscous or conduction region while the convective forcing influences the turbulent flow. Flow structures influence the interfacial temperature more effectively with increasing *TAR* and solid thickness compared with a constant temperature boundary condition. The change of channel flow structures with increasing convective instability is examined and the concomitant change of thermal patterns is quantified. Despite large differences in friction Reynolds and Richardson number between the DNS and atmospheric observations, similarities in the flow features were observed.

Key words: atmospheric flows, buoyancy-driven instability, convection

1. Introduction

Daytime solar heating causes the ground surface to be warmer than the air, resulting in a convectively unstable flow, and this type of atmospheric boundary layer is known as the convective atmospheric boundary layer. The strength of this convective instability mainly depends on the relative magnitude of buoyant production to shear production of turbulence kinetic energy (Richardson number). As the ground becomes warmer, air near the surface becomes more buoyant and the boundary layer becomes

†Email address for correspondence: jkleissl@ucsd.edu
‡Present address: NASA Ames Research Center, Moffett Field, CA 94035, USA.

more unstable. Instability favours the development of turbulent coherent structures that promote and are caused by ascending of near-surface warm air, known as ejection events, and descending of cold air, known as sweep events. The convective boundary layer has a great influence on moisture transport, cloud formation, pollutant transport, and the urban energy balance. In the present study, we defined non-zero finite Richardson number flow as convectively unstable, vanishing Richardson number flow as near-neutral, and infinite Richardson number flow as purely convective flow.

Kaimal & Businger (1970), Wyngaard, Coté & Izumi (1971), Wilczak & Tillman (1980), Wilczak & Businger (1983), Renno *et al.* (2004) and others studied the surface layer which corresponds to of the order of 10 % of the vertical extent of the convective atmospheric boundary layer over flat terrain. The majority of turbulent transport was found to be the result of intermittent events of warm rising air, known as surface layer plumes, and weaker downdraft of cold air from the upper part of the boundary layer. These plumes and downdrafts are manifested as a ramp or sawtooth-like pattern in the timeseries of temperature (Schols 1984; Schols, Jansen & Krom 1985; Gao, Shaw & Paw U 1989) and were also observed in neutral boundary layers (Warhaft 2000; Katul *et al.* 2006*b*). The surface layer plumes have horizontal scales of the order of the surface layer depth, move with the plumes' depth-averaged wind speed and are tilted by wind shear (Wilczak & Tillman 1980).

As the surface layer plumes ascend through the atmosphere, they merge with each other to form thermals in the outer layer of the convective boundary layer, known as the mixed layer in the atmospheric science community. LeMone (1973), Kaimal *et al.* (1976), Lenschow & Boba Stankov (1986), Young (1988*a*,*b*), Cohn *et al.* (1998), Drobinski *et al.* (1998) and Lothon, Lenschow & Mayor (2006) found that with sufficient shear the warm thermals and cold downdrafts form roll vortices in the mixed layer, and create intense turbulence mixing that results in essentially height-constant wind speed, potential temperature and moisture in the outer layer.

These turbulent structures influence the surface temperature of the underlying solid surface. Solid–fluid interfacial temperature fluctuations were observed in the laboratory experiments of neutral channel flow by Hetsroni & Rozenblit (1994), Hetsroni *et al.* (2001) and Gurka, Liberzon & Hetsroni (2004), and in unstable atmospheric flows using single-point infrared sensors, as well as airborne or tower-mounted infrared cameras by Derksen (1974), Schols *et al.* (1985), Gao *et al.* (1989), Katul *et al.* (1998), Ballard, Smith & Koenig (2004), Renno *et al.* (2004), Vogt (2008), Christen & Voogt (2009, 2010) and Garai *et al.* (2013). Time-lapsed animations of spatial fields of interfacial temperature show warm and cold 'structures' on the surface that grow, merge with each other and move along with the mean wind (Garai & Kleissl 2011, 2013). The observed interfacial temperature fluctuations were attributed to be driven by the turbulent eddies, and they are functions of the flow instability and the ground thermal properties (Garai *et al.* 2013).

Many remote sensing applications, e.g. irrigation management, identification of land mines and illegal land-fills etc., often rely on spatial anomalies in a single infrared image, and the turbulence-induced surface temperature fluctuations reduce the effectiveness of the remote sensing technique. Solid–fluid interfacial temperature and heat flux variations are also important in many engineering problems, such as thermal stress in turbine blades induced by secondary flow.

Transient heat conduction models reveal that when two dissimilar materials with different temperatures are in contact, the interfacial temperature depends on the ratio of thermal inertias ($\sqrt{k\rho C_p}$, where ρ, k and C_p are the density, thermal conductivity and specific heat of a material, respectively), and the thickness of the materials

Series	Case	Gr ($\times 10^5$)	TAR	d	Re_τ	Re_c	T_* (K)	T_{**} (K)	L/δ	Ri_τ
A	ssRi	3	1	1	183	65	0.015	0.04	−100.00	−0.02
	sRi	163	1	1	187	305	1.44	0.88	−1.13	−1.77
	base	320	1	1	192	411	3.40	1.62	−0.50	−4.04
	llRi	325	1	1	0	450	∞	1.94	0	∞
B	no-c	325	—	—	193	414	3.46	1.61	−0.50	−4.04
	ssTAR	325	0.01	1	192	411	3.40	1.62	−0.50	−4.04
	sTAR	324	0.1	1	192	411	3.41	1.62	−0.50	−4.04
	sd	324	1	0.1	192	414	3.42	1.61	−0.50	−4.04
	ld	315	1	10	192	410	3.36	1.63	−0.50	−4.04

TABLE 1. Parameters of the DNSs. Series A and B simulations were designed to study the effect of convective instability and solid coupling on the turbulent flow field, respectively. Taking the case labelled 'base' as the reference, the case naming 'c' stands for coupling, 's' stands for small, 'ss' stands for very small, 'l' stands for large, and 'll' stands for very large. Note that for naming the cases in series A, absolute value of Ri_τ was used to define large, small etc.

(Carslaw & Jaeger 1959). Now, for a turbulent flow over a solid wall, heat transport from the surface is essentially driven by diffusion in the conduction sublayer of the turbulent flow. Therefore, the key parameters of the solid–fluid coupled heat transport mechanism are expected to be the solid thickness and the thermal inertia ratio of the solid and fluid, termed the thermal activity ratio (TAR),

$$TAR = \frac{\sqrt{(k\rho C_p)_f}}{\sqrt{(k\rho C_p)_s}} \tag{1.1}$$

where subscripts 'f' and 's' stand for fluid and solid respectively. Tiselj *et al.* (2001) and Balick, Jeffery & Henderson (2003) found that the solid–fluid combinations with large TAR exhibit large interfacial temperature variations. Hunt *et al.* (2003) observed different types of turbulent structures (plumes, puffs) for different solid thermal properties in their direct numerical simulations (DNSs) of purely convectively driven turbulence.

The first objective of this paper is to study the relative role of pressure gradient (mechanical forcing) to buoyancy (thermal forcing), i.e. friction Richardson number (defined in § 2, see series A in table 1), on the turbulent velocity and temperature properties, and coherent structures in a channel flow using DNS. To the best of the authors' knowledge, Iida & Kasagi (1997) are the only authors who combined buoyant convection with a pressure-gradient-driven channel flow DNS. In addition to the higher magnitude of Grashof number (an order higher for the most unstable case), the present simulations differ from the simulations in Iida & Kasagi (1997) by the solid–fluid heat transfer coupling mechanism. A notable finding of Iida & Kasagi (1997) concerning coherent flow structures is that buoyant plumes (shown by instantaneous velocity vectors) inhibit the formation of high- and low-speed near-wall streaks in channel flow. Motivated by this finding, we use a suite of statistical tools (vortex identification, correlation functions and probability distribution functions) to both understand and characterize the coupled thermal and flow structures. The second objective is to improve upon the common approximations of either constant heat flux or constant temperature at the solid–fluid interface by solving the solid-wall

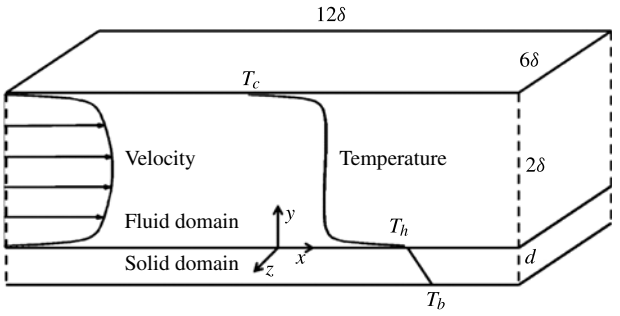

FIGURE 1. Schematic of heated channel flow. The lower wall is hot relative to the upper fluid boundary. Heat conduction in the bottom wall and fluid flow in the channel are solved in a coupled fashion.

conduction and fluid flow simultaneously (see series B in table 1). In other words, both temperature variance and heat flux variance at the interface were captured in a more realistic way in our computational model without constraining the problem with isothermal or adiabatic wall assumptions. While this objective was motivated by the convective atmospheric boundary layer observations, DNS of the atmospheric boundary layer is prohibitive due to a friction Reynolds number (defined in § 2) of 10^7. Therefore, we considered unstable channel flow of smaller friction Reynolds number to gain a better understanding of the solid–fluid coupled heat transport mechanism. The computationally feasible alternative, large eddy simulation, was not considered due to the lack of physical understanding of wall functions for wall bounded flows, especially for convectively unstable configurations. The remainder of the article is arranged in the following manner: §§ 2–6 describe the solid–fluid coupling process, numerical methods, different numerical simulations, analysis of the numerical results, and conclusion, respectively.

2. Problem formulation

The continuity equation, Boussinesq-approximated Navier–Stokes equation and heat transport equation,

$$\frac{\partial u_i}{\partial x_i} = 0, \tag{2.1a}$$

$$\frac{\partial u_i}{\partial t} + u_j \frac{\partial u_i}{\partial x_j} = -\frac{1}{\rho}\frac{\partial p}{\partial x_i} + \nu \frac{\partial^2 u_i}{\partial x_j^2} + g\beta(T - \overline{T})\delta_{i2}, \tag{2.1b}$$

$$\frac{\partial T}{\partial t} + u_j \frac{\partial T}{\partial x_j} = \alpha_f \frac{\partial^2 T}{\partial x_j^2}, \tag{2.1c}$$

respectively, were solved in a pressure-driven channel flow configuration of size $12\delta \times 2\delta \times 6\delta$ in the streamwise, wall-normal and spanwise direction (figure 1), where δ is the fluid channel half-height, x_i are the coordinate directions with $i = 1, 2, 3$ as streamwise (x), wall-normal (y) and spanwise (z) directions, u_i are the streamwise (u), wall-normal (v) and spanwise (w) velocity components, T is the fluid temperature. The variables ρ, ν, β, α_f and g are the density, kinematic viscosity, volumetric thermal expansion coefficient, thermal diffusivity of the fluid (constants under Boussinesq approximation) and gravitational constant, respectively. We assumed the fluid Prandtl

number, Pr, to be unity. The top boundary of the fluid is kept at a fixed temperature, T_c, and the bottom solid–fluid interface has a temperature, T_h, and $T_h > T_c$. The enforced pressure gradient is such that the friction Reynolds number (2.2*d*) would have been 180 without buoyant thermal forcing. Convective instability (Grashof number Gr, (2.2*a*)) is varied by imposing different $T_h - T_c$ for the simulations in Series A. For the purely convective flow, case llRi, a zero pressure gradient was imposed with the highest $T_h - T_c$. The simulated flow field can then be characterized by calculating the friction velocity, convective velocity, friction Reynolds number, convective Reynolds number, friction temperature, convective temperature, Obukhov length and friction Richardson number:

$$Gr = \frac{g\beta(T_h - T_c)(2\delta)^3}{\nu^2}, \tag{2.2a}$$

$$u_* = \sqrt{\frac{\tau_w}{\rho}}, \tag{2.2b}$$

$$v_* = \sqrt[3]{g\beta q_0(2\delta)}, \tag{2.2c}$$

$$Re_\tau = \frac{u_*\delta}{\nu}, \tag{2.2d}$$

$$Re_c = \frac{v_*\delta}{\nu}, \tag{2.2e}$$

$$T_* = \frac{q_0}{u_*}, \tag{2.2f}$$

$$T_{**} = \frac{q_0}{v_*}, \tag{2.2g}$$

$$L = -\frac{u_*^3}{\kappa g\beta q_0}, \tag{2.2h}$$

$$Ri_\tau = -\frac{\kappa g\beta q_0(2\delta)}{u_*^3}, \tag{2.2i}$$

respectively.

The fluid velocity and temperature were initialized with a constant centreline velocity ($\approx(U_b + 2.4u_*)$, where the bulk velocity U_b was estimated from $Re = (U_b 2\delta)/\nu = (Re_\tau/0.09)^{1/0.88}$ for neutral channel flow; see p. 278 of Pope 2000) and bulk temperature ($=(T_h + T_c)/2$) including random disturbances in the fluid domain except at the boundaries. The friction velocity, u_*, was estimated using (2.2*d*) for the desired friction Reynolds number, $Re_\tau = 180$.

After about two eddy turnover times, the fluid domain was coupled with a solid domain of height d. The solid domain thickness is normalized by the heat penetration depth ($\sqrt{\alpha_s\tau}$), where α_s is the solid thermal diffusivity, and the fluid eddy turnover time τ was defined by $\tau = 2\delta/u_*$ and $2\delta/v_*$ for the convectively unstable cases and purely convective case, respectively. The transient 3D heat conduction (2.3*a*) in the solid was solved numerically:

$$\frac{\partial T_s}{\partial t} = \alpha_s \frac{\partial^2 T_s}{\partial x_i^2}, \tag{2.3a}$$

$$T_b = T_h + \frac{(\rho C_p)_f q_0}{k_s}\,\mathrm{d}\sqrt{\alpha_s\tau}, \tag{2.3b}$$

where T_s and α_s are the solid temperature and solid thermal diffusivity, respectively. To ensure that the thermal forcing in the fluid domain remained similar before and after the numerical coupling, the solid domain temperature was initialized using T_h as the solid–fluid interface temperature and q_0 as the wall heat flux ($=-\alpha_f(\mathrm{d}\overline{T}/\mathrm{d}y)$ at $y=0$, where the overbar indicates averaging over the xz cross-section). The solid and fluid domain were then coupled by equating the heat flux, $k_s(\partial T_s/\partial y)_{y=0} = k_f(\partial T_f/\partial y)_{y=0}$, and temperature, $T_{s,y=0} = T_{f,y=0}$, at the interface after each time step. The solid domain bottom temperature was kept fixed at the calculated initial temperature, T_b, (2.3*b*). During the subsequent time evolution of the coupled fluid–solid problem, T_h was allowed to evolve. This was achieved by enforcing the heat flux from the fluid domain at the $(n-1)$th time step on the solid domain at the nth timestep; similarly the temperature from the solid domain at the $(n-1)$th timestep was imposed on the fluid domain at the nth timestep. The solid thermal conductivity and solid thickness were varied to study the effect of solid conduction on the fluid flow. After the start of the solid–fluid coupling, the simulation was run for another 2 eddy turnover times to spin up the solid–fluid coupling. After spin up, the mean and root-mean-square (r.m.s.) interfacial temperature and heat flux at both the solid and the fluid domains were identical, and locally they differed by less than 0.01 %.

3. Numerical technique

The fluid domain was discretized using grid spacing of 7.8, 4.75 (all grid spacings are in wall units) along the streamwise and spanwise directions, respectively. Along the wall-normal direction the grid spacing is 0.18 out to 9 wall units and then uniformly stretched to 5.5 for the highest achievable Re_τ. Consistent with Shishkina *et al.* (2010), these grid spacings were also sufficient for the simulated purely convective case, and led to $320 \times 198 \times 288$ grid points in the fluid domain. The solid domain was discretized using the same grid spacing as the fluid domain resulting in 320×288 grid points in the horizontal direction, and 13–101 grid points in the wall-normal direction depending on the solid domain thickness, d. No-slip and no-penetration boundary conditions were used at the bottom and top boundaries for the fluid domain and periodic boundary conditions were used at the streamwise and spanwise boundaries for both the fluid and solid domains.

The nonlinear advection terms (in the fluid domain) were discretized using the fifth-order Wicker and Skamarock scheme (Wicker & Skamarock 2002), the diffusion times (fluid and solid domain) were discretized using second-order central difference and time advancement (fluid and solid domain) of the variables was performed with third-order low-storage Runge–Kutta scheme (Williamson 1980). A lower-order (first and third) Wicker and Skamarock scheme was used near the wall boundaries. The numerical code was first developed by Raasch & Etling (1991) and applied to study purely convective flow, and the higher-order discretization schemes were added later.

Once the spatially averaged wall shear, the wall heat flux and the solid–fluid interfacial temperature converged, the simulations were continued for an additional 6–7 eddy turnover times, τ (see § 2 for the definition), to gather relevant turbulence statistics.

4. Suite of simulations

Nine simulations were used to study the effects of the relative strength of convective forcing over numerical forcing (series A), and solid conduction (series B) by changing the solid thermal properties (*TAR*) and the solid thickness (d). The friction

Reynolds number (2.2*d*), convective Reynolds number (2.2*e*), friction temperature (2.2*f*), convective temperature (2.2*g*), Obukhov length (2.2*h*) and friction Richardson number (2.2*i*) for each simulation are given in table 1.

For reference, we also simulated convectively unstable flow without any solid coupling (case no-c). With the addition of buoyancy, the flow becomes more turbulent compared with the neutral case, hence Re_τ increases. The Obukhov length, L, a virtual height above which buoyant production dominates shear production of turbulence kinetic energy, decreases in magnitude with the increase in Gr, and hence the friction Richardson number ($Ri_\tau = 2\delta/L$) increases. We have used typical near-wall scaling laws for normalization of the variables and the normalized variables are denoted by subscript '+' for the convectively unstable case (all cases except ssRi and llRi) and near-neutral case (case ssRi). As the friction Reynolds number is zero for purely convective turbulence (case llRi) convective velocity, and temperature scales and the thermal boundary layer depth ($=(T_h - T_c)/(-2\mathrm{d}\overline{T}/\mathrm{d}y|_{y=0})$, as defined by Shishkina *et al.* 2010) were used for normalization and the normalized variables are denoted by superscript '++'.

The numerical fluid–solid coupling procedure has some effect on the Gr. With increasing TAR and d, the solid–fluid interfacial temperature decreases from the initial temperature (T_h) in case no-c, resulting in a drop in the Gr. In the numerical simulations of Rayleigh–Bénard convection (RBC), Verzicco & Sreenivasan (2008) also found that the wall temperature decreased when a constant wall heat flux boundary condition was used instead of constant wall temperature and inferred that scatter in Nusselt numbers amongst different experimental studies of RBC was due to the use of different solid materials. As the present interfacial boundary condition is in-between the two extreme boundary conditions, isothermal and isoflux, a decrease in the interfacial temperature with TAR and thickness is consistent with this observation.

5. Results

Since the novelty of our paper not only lies in the solid–fluid coupling, but also the simulation of convectively unstable channel flow, both the effect of the friction Richardson number and the solid–fluid coupling will be discussed in the following subsections.

5.1. *Effect of friction Richardson number (series A)*

Instantaneous snapshots of temperature (figure 2*b–d*) show warm and cold regions at the solid–fluid interface. These regions are aligned with the flow structures. The interfacial temperature patterns and the turbulent coherent structures are different for the unstable, near-neutral and purely convective case. While in the unstable base case (figure 2*b*) the strongest turbulent ejection and sweep structures tend to align one after another forming streamwise roll vortices (Iida & Kasagi 1997), in the near-neutral case (figure 2*c*) the interfacial temperature is influenced by the low- and high-speed streaks and skin friction structure for a neutral channel flow (Kim, Moin & Moser 1987), and for the purely convective case (figure 2*d*) the interfacial temperature structures tend to be cell-like (Verzicco & Sreenivasan 2008). Despite order of magnitude differences in the friction Reynolds numbers, large-scale flow structures (roll vortices) for convectively unstable flow are similar to those observed in the convective atmospheric boundary layer with shear (LeMone 1973; Kaimal *et al.* 1976; Lenschow & Boba Stankov 1986; Young 1988*a*,*b*; Cohn *et al.* 1998; Drobinski *et al.* 1998; Lothon *et al.* 2006). Hetsroni & Rozenblit (1994) observed similar elongated interfacial temperature structures in an open channel neutral flow experiment with $Re_\tau = 290$–500.

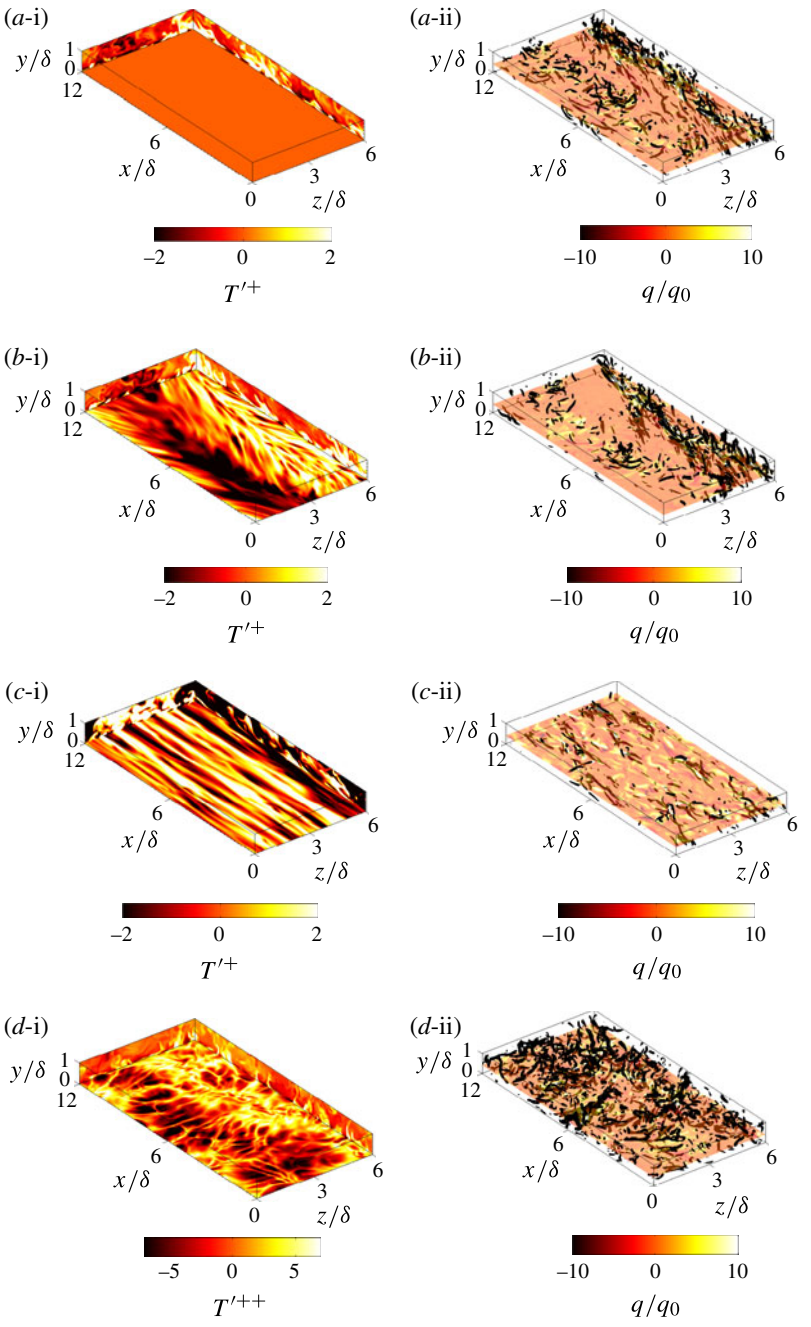

FIGURE 2. (Colour online) Visual examination of interfacial temperature and vortical structures. Instantaneous snapshots of (i) temperature at the domain boundaries; and (ii) strong vortex cores (identified using isosurfaces of swirling strength) with total heat flux at $y = 0.4\delta$ for (a) case no-c (no coupling) with interfacial temperature, (b) the base case, (c) case ssRi with very small convective forcing and (d) case llRi with only convective forcing without streamwise pressure gradient. The cut-off value for swirling strength was $3.5 \times 10^{-2}(\partial u/\partial y)^{-2}_{y=0}$ for cases no-c, base and ssRi, and $5.5 \times 10^{-4}(v_*^2/\nu)^{-2}$ for case llRi.

The swirling strength criteria (Zhou *et al.* 1999; Pierce, Moin & Sayadi 2013) were employed for the identification of vortex structures (figure 2(ii)). Strong vortex cores are predominantly in the updraft regions (inferred from positive T') compared with the downdraft regions (inferred from negative T'). Details of these turbulent structures and their implication on the interface temperature will be discussed in the following sections.

5.1.1. *Mean profiles*

The mean streamwise velocity increases linearly with wall-normal distance in the viscous sublayer region, $y^+ < 5$ (figure 3*a*). Similarly the temperature decreases in the conduction sublayer with a slope of Pr (see figure 1 of Wang, Castillo & Araya (2008) for definitions of the different thermal sublayers); see figure 3(*b*). Note that as the molecular properties of the fluid determines the flow in the viscous and conduction sublayer, their thicknesses are similar due to unity Pr fluid. In the log law region, convective instability causes enhanced turbulent mixing. Thus, the velocity (Kim *et al.* 1987) (5.1) and temperature (Kader 1981) (5.2) profiles deviate from the neutral log law formulations:

$$u^+ = \frac{1}{\kappa} \ln y^+ + 5.5. \tag{5.1}$$

$$T^+ = 2.12 \ln y^+ + ((3.85 Pr^{1/3} - 1.3)^2 + 2.12 \ln Pr) \tag{5.2}$$

for all cases except ssRi and llRi. Also note that the log law formulation is inapplicable for case llRi, due to zero friction velocity. Instead they follow Monin–Obukhov similarity theory (Monin & Obukhov 1954):

$$u^+ = \frac{1}{\kappa} (\ln y^+ + \psi_m(y/L)) + C_m, \tag{5.3}$$

$$T^+ = \frac{1}{\kappa} (\ln y^+ + \psi_h(y/L)) + C_h, \tag{5.4}$$

where $\psi_m(y/L)$ and $\psi_h(y/L)$ are the stability correction factors for unstable conditions in the streamwise velocity and temperature, respectively, and are defined by

$$\psi_m\left(\frac{y}{L}\right) = -2 \ln\left(\frac{1+X}{2}\right) - \ln\left(\frac{1+X^2}{2}\right) + 2 \arctan X - \pi/2, \tag{5.5}$$

$$\psi_h\left(\frac{y}{L}\right) = -2 \ln\left(\frac{1+X^2}{2}\right), \tag{5.6}$$

respectively, where $X = (1\text{–}16(y/L))^{1/4}$ (Paulson 1970), derived using Businger–Dyer relationships (Högström 1988). As Monin–Obukhov similarity theory was derived for the surface layer of the atmospheric boundary layer and the associated profile equations contain additional parameters that describe the roughness, (5.3) and (5.4) were modified using additive constants C_m and C_h for the present channel flow configuration. The non-dimensional mean temperature T^+ in (5.2) and (5.4) are defined by $|(\overline{T} - \overline{T}_{wall})/T_*|$, where $\overline{T}_{wall}$ is the nearest wall temperature. The mean temperature profile for case llRi compares well with the literature on RBC (Ahlers, Grossmann & Lohse 2009). Also note that the normalizations differ for purely convection-driven turbulence (case llRi), as described in § 4. For the near-neutral case (case ssRi), the log law profile was recovered for the mean velocity, but neither the log law profile nor Monin–Obukhov similarity (with $\psi_h = 0$) describe the mean temperature profile. Since we do not observe a similar discrepancy for convectively unstable flow which exhibits stronger turbulence level in the bulk region compared with neutral flow, we speculate that the turbulence for $Re_\tau = 183$ may not be strong

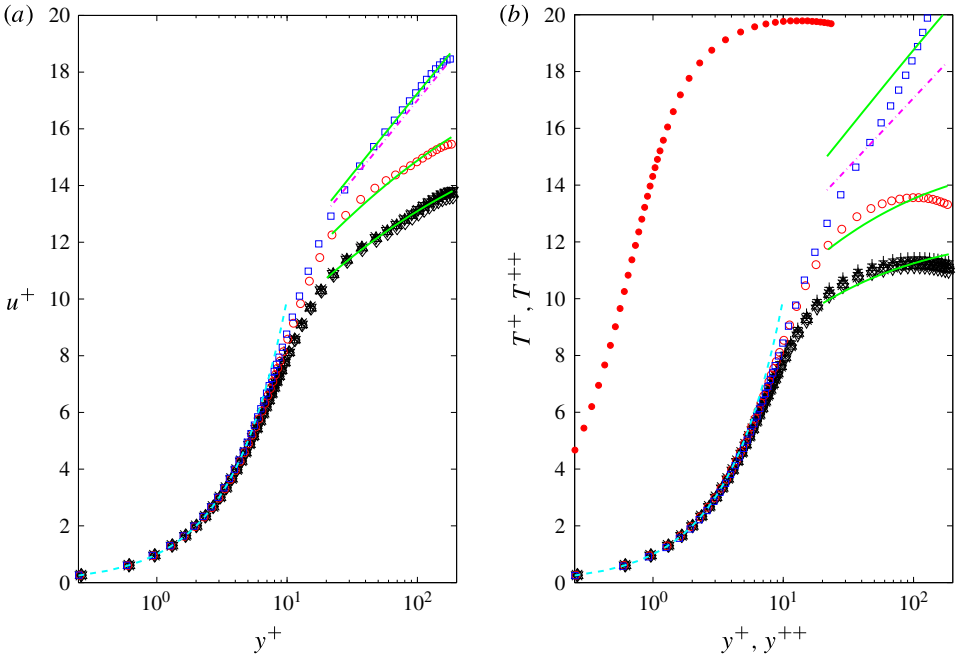

FIGURE 3. (Colour online) Comparison of mean (*a*) streamwise velocity and (*b*) temperature profiles for cases no-c (black prism), base (black cross), ssTAR (black plus), sTAR (black star), sd (black upper triangle), ld (black lower triangle) (all black symbols fall on top of each other), sRi (red circle), ssRi (blue square) and llRi (filled red circle) with viscous/conduction sublayer linear profile (cyan broken line), neutral log law (magenta solid dotted line) and Monin–Obukhov similarity law for unstable flow (green solid line).

enough to homogenize the temperature in the bulk region. The mean solid temperature increases linearly with distance from the solid–fluid interface and the slope depends on the solid thermal properties and thickness (not shown).

The C_m (in (5.3)) and C_h (in (5.4)) were estimated using a least-squares method for the $y^+ > 20$ and $y < \delta$ regions (table 2) and for smaller Richardson number (case ssRi) the neutral channel flow values are recovered. The accuracy of the estimated values of C_m and C_h suffers from the limited extent of the log layer region at small Re_τ. Note that for neutral conditions Jiménez (2012) stated that for a substantial log region in a turbulent wall bounded flow Re_τ should be greater than 750, but this Re_τ requirement changes with the strength of convective instability.

5.1.2. *The r.m.s. profiles*

The r.m.s. profiles of velocity for convectively unstable flows are significantly different from the profiles for the near-neutral and purely convective channel flow (figure 4*a–c*). In a near-neutral channel flow (case ssRi), u' is the most energetic component, reaching a maximum of $\sigma_u = 2.65u_\tau$ at $y^+ = 14$, and in the outer region ($0.2 < y/\delta < 0.85$) all three velocity components decreases linearly, consistent with Kim *et al.* (1987) and Moser, Kim & Mansour (1999). For purely convectively driven turbulence (case llRi) the r.m.s. of the horizontal velocities (u' and w') peak at the top of thermal boundary layer, and the r.m.s. of the wall-normal velocity (v') peaks at the middle of the channel.

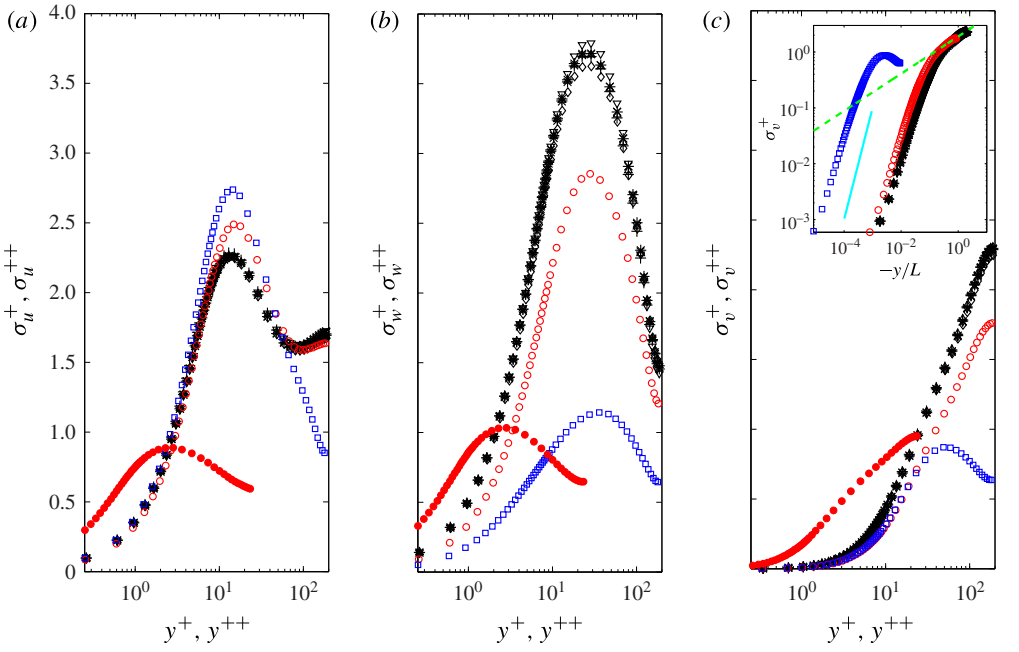

FIGURE 4. (Colour online) Normalized r.m.s. profiles of (*a*) streamwise, (*b*) spanwise and (*c*) wall-normal velocity components for cases no-c (black prism), base (black cross), ssTAR (black plus), sTAR (black star), sd (black upper triangle), ld (black lower triangle), sRi (red circle), ssRi (blue square) and llRi (filled red circle). The inset shows the comparison of wall-normal r.m.s. velocity for unstable and near-neutral cases with the similarity formulation by Wyngaard *et al.* (1971) (green broken line) and y^{+2} slope line (cyan solid line).

Case	C_m (—)	C_h (—)
no-c	4.4	4.5
base	4.4	4.5
ssTAR	4.4	4.5
sTAR	4.4	4.5
sd	4.4	4.5
ld	4.4	4.5
sRi	5.2	5.3
ssRi	5.5	7.0
llRi	—	—

TABLE 2. Best fit values of the offsets in the velocity and temperature profiles (5.3) and (5.4) for different simulated cases.

For the convectively unstable flows (all cases except ssRi and llRi) the spanwise velocity component w' is the most energetic below $y/\delta = 0.6$. The increase in the spanwise r.m.s. velocity with increase in convective instability, can be explained by examining the pressure rate-of-strain tensor, $R_{ij} = \overline{(p'/\rho)(\partial u_i'/\partial x_j) + (\partial u_j'/\partial x_i)}$ (a measure of energy redistributive effects of fluctuating pressure). For the turbulence kinetic energy balance, the trace of R_{ij} becomes zero due to the continuity equation,

but for the balance of individual $\overline{u'^2}$, $\overline{v'^2}$ and $\overline{w'^2}$, R_{ij} quantifies how fluctuating pressure redistributes the energy amongst $\overline{u'^2}$, $\overline{v'^2}$ and $\overline{w'^2}$ (Pope 2000). Unlike the near-neutral case (case ssRi) where energy is transferred from the streamwise component to both spanwise and wall-normal components by pressure fluctuations, in the unstable cases the fluctuating pressure transfers energy from both the streamwise and wall-normal components to the spanwise component (not shown). For the unstable cases the streamwise r.m.s. velocity peaks where the shear production term in the turbulent kinetic energy budget peaks, as generally observed in wall-bounded flow (Pope 2000), and both peak locations for streamwise r.m.s. velocity and shear production move towards the solid–fluid interface as the magnitude of Ri_τ increases. Similar observations were also made by Iida & Kasagi (1997) for $Re_\tau = 150$ and $Gr \approx 10^6$. With the exception of cases ssRi and llRi, we do not observe a decay of u' in the $y/\delta > 0.25$ region for the convectively unstable cases; instead u' r.m.s. remains constant ($\sim 1.6u_\tau$) in this region. The r.m.s. of the wall-normal component v increases as y^{+2} in the viscous sublayer, but due to the increase in the buoyant production term of the turbulence kinetic energy budget in the outer region, it peaks at the channel half-height for the convectively unstable cases (inset of figure 4*c*). This increase in v in the $y/\delta > 0.25$ region can be successfully described by $\overline{v^2}^{1/2}/u_* = 1.9(-y/L)^{1/3}$ (Wyngaard *et al.* 1971).

The fluid temperature r.m.s. value peaks in the buffer region, at a similar location where the streamwise r.m.s. velocity peaks (right panel of figure 5). This similarity is due to the unity Pr fluid. In the convectively unstable cases (all cases except ssRi and llRi), the decay of the fluid temperature r.m.s. between $0.2 < y/\delta < 1$ can also be described by similarity theory: $\overline{T'^2}^{1/2}/T_* = 0.95(-y/L)^{-1/3}$ (Wyngaard *et al.* 1971). For purely convective turbulent flow (case llRi), the fluid temperature r.m.s. also decreases as $y^{-1/3}$ beyond the thermal boundary layer region. On the other hand, for near-neutral flow (case ssRi) the fluid temperature r.m.s. value oscillates around 3 due to the non-zero production term of the fluid temperature variance budget equation at the midchannel. Similar results for the neutral flow were reported by several authors, and this behaviour was attributed to the asymmetric mean fluid temperature profile (Johansson & Wikström 1999; Armenio & Sarkar 2002; Morinishi, Tamano & Nakamura 2007). De Bruin, Kohsiek & Van Den Hurk (1993) also reported that the fluid temperature r.m.s., when normalized by the friction temperature, asymptotes to three in large Re_τ atmospheric boundary layers for near-neutral conditions. The effect of the asymmetry in the mean fluid temperature profile on the fluid temperature variance production term gets nullified for the convectively unstable and purely convective cases, due to the buoyancy enhanced turbulent mixing.

5.1.3. *Temperature probability density function*

The probability density function (p.d.f.) of the fluid temperature fluctuations as a function of wall-normal distance is now examined to gain insight into the manifestation of coherent structures (figure 6). The conditionally averaged wall-normal velocity v is also shown. The wall-normal velocity and the fluid temperature fluctuations are highly correlated outside the conduction region.

In the region $0.1 < y/\delta < 1$, the temperature fluctuation p.d.f.s for the convectively unstable and purely convectively driven cases show (i) a short negative tail with high-probability events and (ii) a long positive tail. The high-probability density region moves towards lower temperatures near $y/\delta = 0.1$, because of the increase in the temperature difference of cold sweeps versus the warm background. The

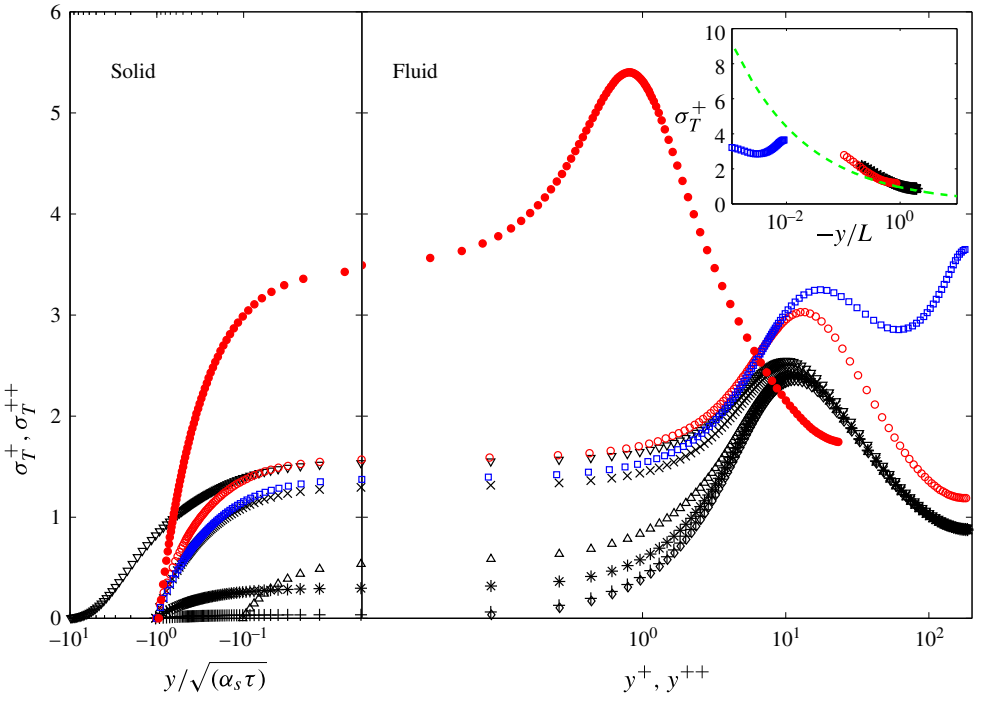

FIGURE 5. (Colour online) The normalized r.m.s. temperature profile of the solid (left panel) and the fluid (right panel) for cases no-c (black prism), base (black cross), ssTAR (black plus), sTAR (black star), sd (black upper triangle), ld (black lower triangle), sRi (red circle), ssRi (blue square) and llRi (filled red circle). The inset of the figure shows the fluid temperature standard deviation in the $y^+ > 20$ region for unstable and near-neutral cases with the similarity theory by Wyngaard *et al.* (1971) (green broken line).

magnitude of the wall-normal velocity associated with sweep events also decreases with the proximity to the wall. On the positive T' side, intermittent ejection events result from the fluid heating near the warm bottom wall and upward acceleration due to buoyancy. While the upper half of the channel is not shown in figure 6, the characteristics of the p.d.f. for $1 < y/\delta < 1.9$ are similar as in the lower half of the channel, except that near the top the positive temperature fluctuation region assumes the characteristics of the negative temperature fluctuation region near the warm bottom wall. Since the fluid temperature acts as a passive scalar for the near-neutral case (case ssRi in figure 6*d*), the fluid temperature p.d.f. in the region $y/\delta > 0.1$ becomes less skewed (positive and negative tails exhibit similar lengths) irrespective of wall-normal distance. On the other hand, the temperature p.d.f. changes to a Gaussian behaviour inside the conduction region ($y < 0.03\delta$) for all cases, since there the molecular diffusion process is dominant over the turbulent transport. These characteristics were also observed in the atmospheric convective boundary layers (Chu *et al.* 1996; Garai & Kleissl 2013).

5.1.4. *Conditional averaging*

The above-mentioned fluid temperature p.d.f. characteristics can be further explained by studying the turbulent structures using conditional averaging. Different events were

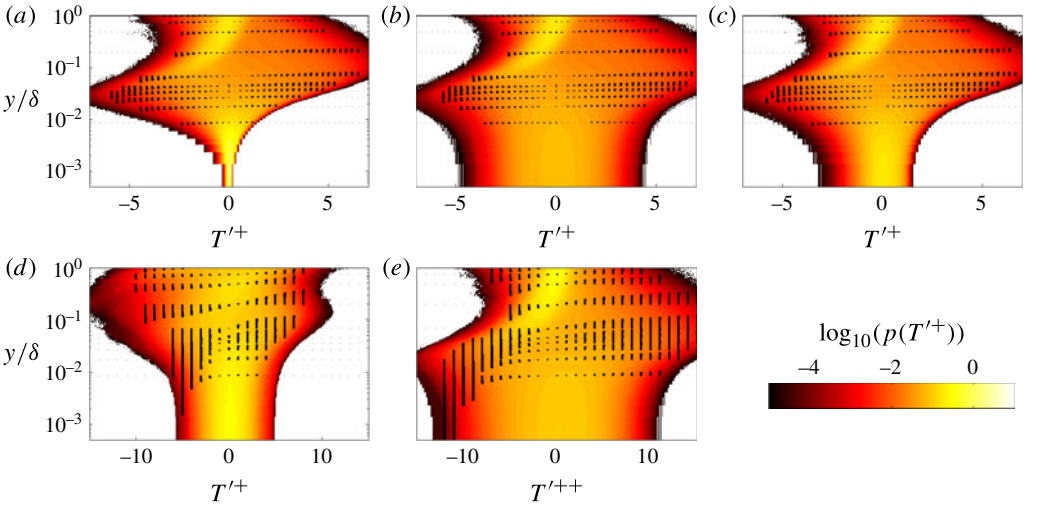

FIGURE 6. (Colour online) Fluid temperature p.d.f.s versus wall-normal distance for case (*a*) ssTAR, (*b*) base, (*c*) sd, (*d*) ssRi and (*e*) llRi. The black vectors represent conditionally averaged normalized wall-normal velocity over the temperature fluctuation bin. The largest magnitude of the velocity vectors is $5u_*$ for cases ssTAR, base, ld, $1.5u_*$ for case ssRi and $2v_*$ for case llRi.

identified using thresholds as follows: (i) the total heat flux $(-\alpha_f(\partial T/\partial y) + vT') \geqslant q_0$, (ii) the absolute value of the wall-normal velocity $\geqslant u_*$ (for the purely convective case v_* was used instead) and (iii) the horizontal cross-sectional area $\geqslant 0.028\delta^2$ at a given time. The ejection and sweep events were differentiated by the sign of the wall-normal velocity. The search for coherent structures that meet the conditions was repeated for different time instants with a minimum separation of 0.2τ, since the temporal decorrelation length at the midchannel height was 0.4τ for the base case.

For $y/\delta < 0.1$, sweeps and ejections could not be identified by the previously mentioned criteria, as the wall-normal velocity fluctuations in this region are small (figure 4). With increase in wall-normal distance, the number of ejection and sweep events increases, and the numbers plateau when $y > 0.2\delta$. Also the turbulent heat transport mechanism dominates the molecular heat transport when $y > 0.2\delta$. For unstable cases, the ejection and sweep events cover only approximately 20 % and 15 % of the horizontal domain respectively, but together they are responsible for almost all (approximately 100 %) of the heat transport. The ejection events are responsible for most of the heat transport (approximately 75 %) compared with the sweep events (approximately 25 %) near the bottom wall (at 0.2δ), but the relative contributions of the sweeps increase with wall-normal distance. In the midchannel region both ejection and sweep events contribute equally (approximately 45 %) to heat transport.

At $y = 0.2\delta$, most of the temperature variance occurs due to the ejection events (approximately 50 %) compared with the sweep events (approximately 10 %). At $y = 0.7\delta$, the ejection and sweep contributions increase to approximately 70 % and 25 % of temperature variance, respectively, and then the ejection contributions decrease, whereas the sweep contributions continue to increase up to channel half-height (δ). Ejection and sweep events contribute equally (approximately 35 % each) to the wall-normal velocity variance irrespective of wall-normal distance.

On the other hand for case ssRi, the near-neutral case, ejection and sweep events cover only approximately 5 % of the horizontal domain and contribute less towards the heat flux (approximately 50 % for ejection events; and approximately 25 % at $y = 0.2\delta$ to 50 % at $y = \delta$ for sweep events), temperature (approximately 10 % for both ejection and sweep events) and wall-normal velocity (approximately 40 % for ejection and approximately 20 % for sweep events) variance. For case llRi, the purely convective case, ejection and sweep events cover approximately 10 % of the horizontal domain, and contribute similarly toward the heat flux, temperature and wall-normal velocity variance, compared with the unstable cases. The criteria used to identify turbulent events affect the quantitative statistics provided here, but the qualitative behaviour remains unaltered. Despite the differences in Re_τ for the present convectively unstable simulations and atmospheric convective boundary-layer observations, similar conditional statistics were observed (Kaimal & Businger 1970; Kaimal *et al.* 1976; Garai & Kleissl 2013).

Next we studied 3D structures of the ejection and sweep events identified at $y = 0.4\delta$ for base, ssRi and llRi cases. The streamwise, spanwise and wall-normal distances of the turbulent structures were normalized by their streamwise length at $y = 0.4\delta$ and scaled such that '0' marks the start of an event in the streamwise and spanwise directions and '1' marks the end of an event in the streamwise direction. Events that extended to the horizontal boundaries of the numerical domain were excluded.

In the unstable flow cases, as the cold fluid parcels approach the solid–fluid interface during sweep events (figure 7(i)), they encounter a warmer background causing the temperature difference to increase. Consequently the fluid temperature near the bottom surface decreases (figure 7(i)), resulting in high probability of negative temperature (figure 6). The wall-normal velocity of the cold fluid parcel goes to zero as it approaches the wall due to the no-penetration boundary condition. This results in a diverging flow pattern in horizontal directions during sweep events near the bottom wall (figure 7(ii)). On the other hand, ejection events (figure 7(iii)) are caused by fluid heating near the bottom wall. With sufficient buoyancy, the warm fluid parcel then ascends through the channel and causes a converging flow pattern in the horizontal directions (figure 7(iv)). The largest ejections and sweeps have streamwise lengths of approximately 6δ for both $Ri_\tau = -4.04$ and -1.77; and ejections are smaller in the spanwise direction than sweeps.

Fluid temperature acts mostly as passive scalar for the near-neutral case (case ssRi) and thus the identified ejection and sweep events (figure 7*c*) resemble the near-wall low- and high-momentum regions for neutral channel flow. The streamwise and spanwise lengths of the largest ejection and sweep events are of similar length of only 1.5δ. The horizontal divergence and convergence flow patterns triggered by the ejection and sweep events become weaker.

For case llRi the absence of shear leads to cellular-like structures with maximum streamwise and spanwise lengths of approximately 2δ (figure 7*d*). The conditionally averaged fluid temperatures of ejection and sweep events show similar behaviour with wall-normal distance compared with the unstable cases. The horizontal convergence and divergence flow patterns for purely convective flow are the strongest amongst the studied cases.

5.1.5. *Three-dimensional spatial temperature cross-section*

The typical size of the turbulent structures at a given instant was studied by considering cross-correlation of the fluid temperatures, ρ_{TT} (5.7):

$$\rho_{TT}(\Delta x, y - y_0, \Delta z) = \frac{\langle T'(x, y_0, z, t)T'(x + \Delta x, y, z + \Delta z, t)\rangle}{\langle T'(x, y_0, z, t)T'(x, y_0, z, t)\rangle}, \tag{5.7}$$

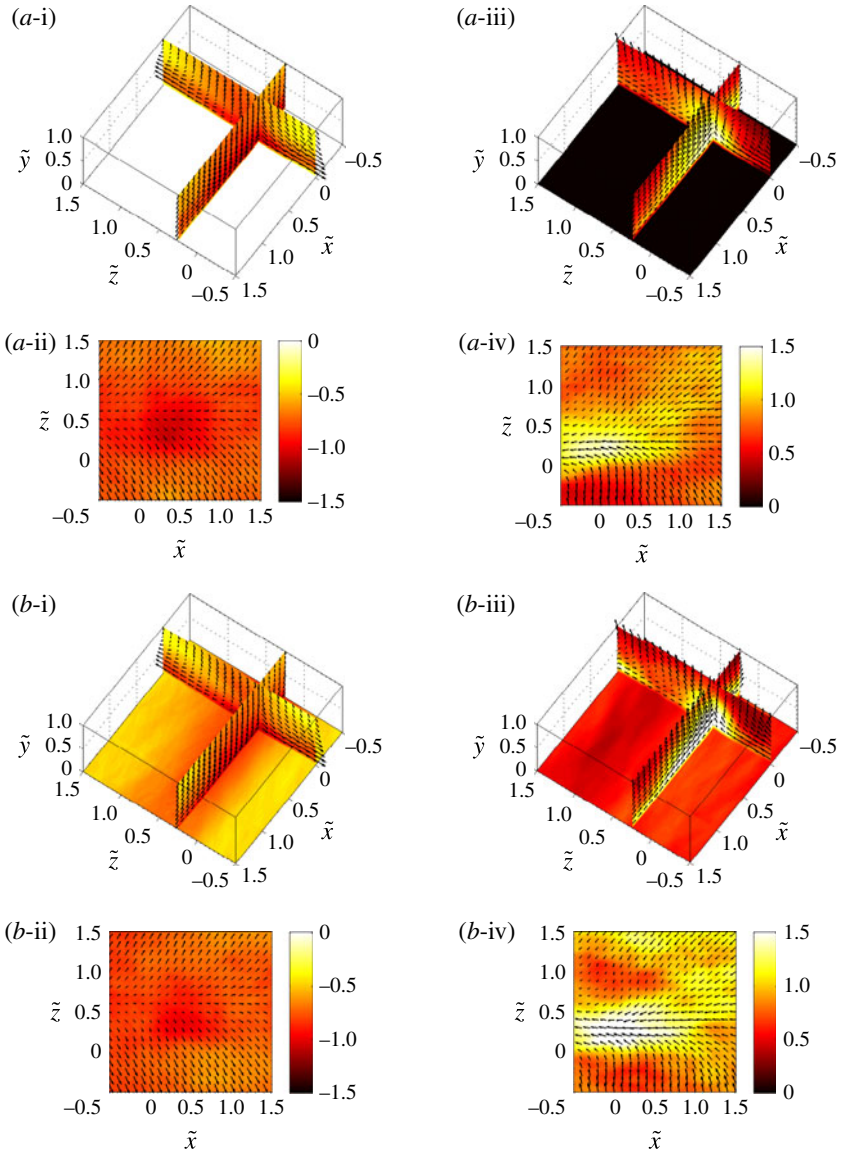

FIGURE 7. For caption see next page.

at different wall-normal distances with respect to the fluid temperature at a wall-normal distance $y_0 = 0.4\delta$ (figure 8). This value of y_0 was chosen to study the average size of the ejection and sweep events (§ 5.1.4). The angled brackets in (5.7) represent averaging over x, z and t. For the isosurface a correlation coefficient of e^{-1} was chosen, since the autocorrelation function decays exponentially for most turbulent variables. The structure size depends on this value, but qualitative features are not sensitive to the choice of threshold.

The 3D structure of temperature correlation for the unstable cases (figure 8*b*) have some distinct characteristics: (*a*) in the outer region the spanwise extent of the turbulent structures is smaller than the streamwise extent and these structures have a longer tail in the upstream direction, (*b*) in the viscous/conduction sublayer,

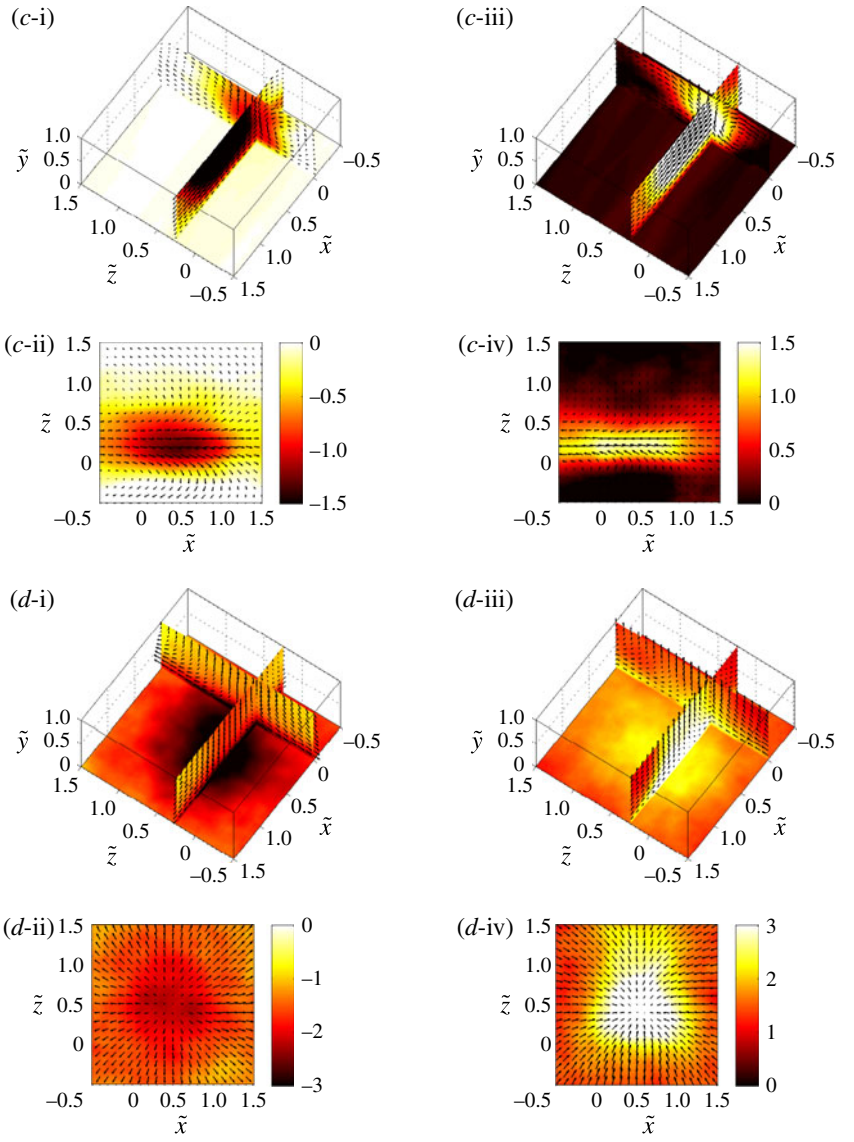

FIGURE 7. (cntd). (Colour online) Three-dimensional structure and $\tilde{x}\tilde{z}$ cross-sectional view at $\tilde{y} = 0.25$ of the conditionally averaged (i and ii) sweep events and (iii and iv) ejection events for case (*a*) no-c, (*b*) base, (*c*) ssRi and (*d*) llRi. The colour scale represents the conditionally averaged temperature, and the black vectors represent the conditionally averaged in-plain fluid velocity. Curly overbars represent distance normalized by the streamwise lengths of the ejection (sweep) events. Note that the colour scales for the sweep and ejection events are different.

the upstream and downstream spatial extents are similar and (*c*) shear near the wall tilts the temperature correlation structures in the flow direction. Strong horizontal convergence and divergence flow patterns are responsible for the increase in the spatial extent of the high-correlation region near the surface.

For the near-neutral flow (case ssRi, figure 8*c*), the influence of buoyant forcing vanishes and the temperature behaves like a passive scalar. Thus, the wall-normal

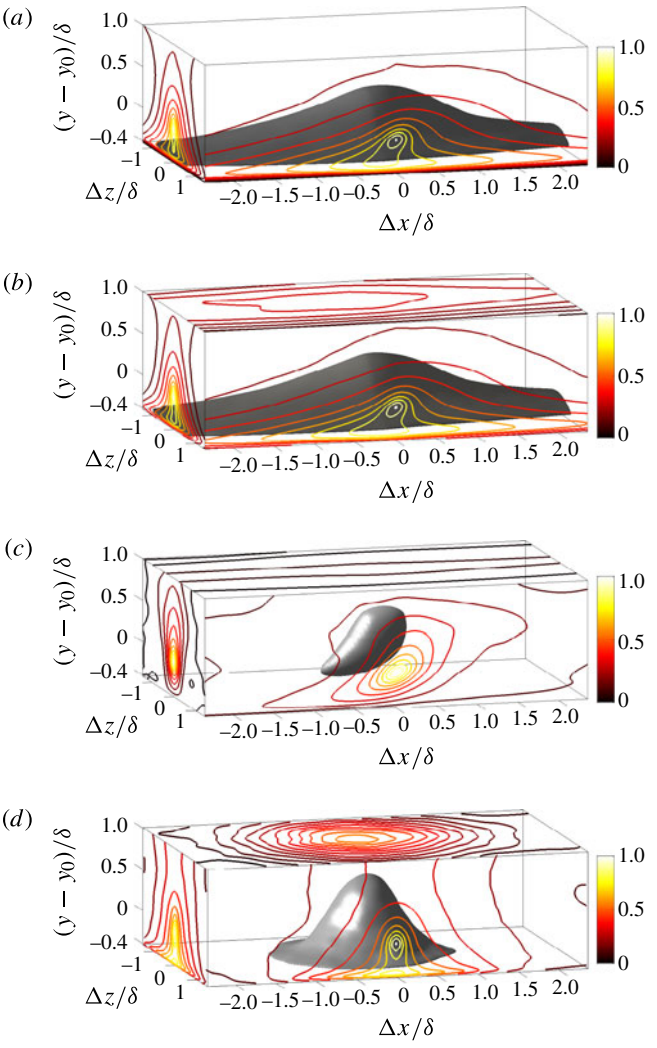

FIGURE 8. (Colour online) Plot of the spatial cross-correlation of temperature, ρ_{TT} (5.7), with respect to temperature at a reference height of $y_0 = 0.4\delta$. The correlation is shown for case (*a*) no-c, (*b*) base, (*c*) ssRi with near-neutral conditions and (*d*) llRi with purely convective forcing. The black isosurface at a value of cross-correlation $= e^{-1}$ is shown to help infer the 3D structure of correlation function. The contours in the x–y, y–z and x–z plains show cross-correlations at $\Delta z = 0$, $\Delta x = 0$ and $y = 0$, respectively, and are displaced for visual clarity. Negative Δx denotes the upstream region and vice versa. There is no contour line on the top surface of (*a*), as the interfacial temperature function is zero for case no-c.

velocity is less effective in transporting fluid temperature fluctuations compared with the convectively unstable cases. This results in a smaller length scale of the correlation function in all three directions.

For the purely convective flow (case llRi, figure 8*d*), the horizontal extent of the high-correlation region is smaller than that of the unstable flow (case base, figure 8*b*). In the high-correlation region the signature of convergence and divergence flow

patterns in the horizontal cross-section near the wall is also present in the purely convective flow, but with a smaller wall-normal extent.

The tilt of the temperature high-correlation region depends on both the shear and buoyancy forcing. In a flow with pure shear, $\mathrm{d}U/\mathrm{d}y$, the principal axes of strain are inclined at 45° with respect to the horizontal direction (x). Thus, for the neutral flow, the correlation region near the surface is tilted by approximately 45° since the near-wall turbulence is driven by the wall shear. For the purely convective flow, the high-correlation region is oriented normal to the wall, as buoyancy forcing is the only mechanism for vertical mixing. For unstable flow, the tilt is in-between these two extremes, depending on the relative strength of buoyancy and shear: specifically tilt angles are 57° and 50° for $Ri_\tau = -4.04$ and -1.77, respectively. In the bulk region away from the wall the turbulent structures tend to be more normal to the wall since buoyancy increases while wall shear decreases in the bulk region. When the tilt of the temperature high-correlation region is compared with the streamwise velocity high-correlation region (not shown), the temperature structures have greater tilt compared with the streamwise velocity structures. The streamwise velocity structures are tilted by 12°, 30°and 35° for ssRi, sRi and base cases, respectively, consistent with the observations by Antonia, Abe & Kawamura (2009) for neutral channel flow.

5.2. *Effect of solid–fluid coupling (series B)*

The solid thermal properties and thickness of the solid domain do not influence the mean fluid velocity (figure 3*a*) and fluid temperature (figure 3*b*), except for a small change in the interfacial mean temperature (described in § 4); and turbulent velocity fluctuations (figure 4). They only affect the fluid temperature fluctuations in the $y^+ < 20$ region (figure 5) and interfacial temperature structures (figure 2). The normalized interfacial temperature varies spatially by approximately ±14 for the case base (figure 2*b*) and by ±0.1 for case ssTAR (figure 2*c*).

The increase in the variance of the interfacial temperature and of the conduction sublayer region fluid temperature variances with *TAR* was also observed by Tiselj *et al.* (2001). As the solid thermal inertia ($\sqrt{(k\rho C_p)_s}$) increases, the interfacial temperature structures are more effectively homogenized through conduction and internal heat storage. Thus, the solid–fluid coupled heat transport mechanism behaves similar as for an isothermal boundary condition with correspondingly high surface heat flux variation for $TAR \to 0$; and as for an isoflux boundary condition with high surface temperature variation for $TAR \to \infty$ (table 3). With increasing *TAR*, large turbulent structures more effectively imprint on the fluid–solid interface relatively to small flow structures. Small-scale fluctuations fail to imprint on the surface, but the definition of small depends on the *TAR* as the thermal inertia acts like a physical filter on the interfacial temperature.

In addition to *TAR*, the thickness of the solid domain also influences the spectral decay of fluid temperature fluctuations in the conduction sublayer. The isothermal boundary condition imposes zero temperature fluctuation at the solid bottom boundary and thus the thickness of solid domain influences the interfacial heat transport process. The mechanism is related to the heat penetration depth of the turbulent eddy footprints. With a thinner solid ($d = 0.1$), the large turbulent temperature fluctuations cannot penetrate the solid, because they are damped by the bottom boundary of the solid. Note that d is the height of the solid domain normalized by the heat penetration depth, $\sqrt{\alpha_s \tau}$, defined in § 2. On the other hand, for a thicker solid ($d \gg 1$) the solid–fluid coupled heat transport mechanism becomes independent of the bottom boundary of the

Case	$\sigma_{T^+_{y=0}}$ (—)	σ_{q_0}/q_0 (—)
no-c	0	0.39
ssTAR	0.03	0.39
sTAR	0.30	0.36
base	1.30	0.20
sd	0.56	0.29
ld	1.54	0.20
sRi	1.58	0.19
ssRi	1.39	0.22
llRi	3.46	0.23

TABLE 3. The solid–fluid interfacial temperature and heat flux r.m.s. as a function of solid thermal properties, height of the solid domain and flow instability. For case llRi, the interfacial temperature r.m.s. is normalized by the convective temperature scale.

solid. This behaviour for thin solids will change if one assumes an isoflux boundary condition at the solid bottom boundary. With an isoflux boundary condition at the bottom boundary of the solid domain, Tiselj *et al.* (2001) found that for thin solids interfacial temperature fluctuations increased for neutral conditions. For a thick solid ($d \gg 1$), however, the isothermal or isoflux boundary condition will not matter, as the turbulent eddy heat penetration depth will be sufficiently smaller than the thickness of the solid domain.

As the buoyant production term of the turbulent kinetic energy budget is essentially independent of *TAR* and solid domain thickness, spectra and hence the variances of the velocity components (u', v', w') do not change.

Hence, the fluid temperature p.d.f. in the conduction sublayer (figure 6*a–c*) changes with the solid–fluid coupling process. Larger *TAR* and d increase the spread of the temperature p.d.f. and decrease the thermal diffusion, $\alpha_f(\mathrm{d}^2\overline{T'^2}/\mathrm{d}y^2)$, and thermal dissipation, $\alpha_f\overline{(\partial T'/\partial x_i)(\partial T'/\partial x_i)}$ terms in the following temperature variance budget equation:

$$0 = -\frac{\mathrm{d}\left(\overline{vT'^2}/2\right)}{\mathrm{d}y} + \alpha_f\frac{\mathrm{d}^2(\overline{T'^2}/2)}{\mathrm{d}y^2} - \overline{vT'}\frac{\mathrm{d}\overline{T}}{\mathrm{d}y} - \alpha_f\overline{\frac{\partial T'}{\partial x_i}\frac{\partial T'}{\partial x_i}}. \tag{5.8}$$

As described previously, the solid–fluid coupling only influences the fluid temperature in the conduction sublayer through the thermal diffusion process, while the characteristics of turbulent coherent structures (figure 7) remain unaltered. Here *TAR* and d only influences the imprint of the turbulent structures on the solid–fluid interface (figure 7*a* and *b*) resulting in a change in the cross-correlation between interfacial temperature and fluid temperature (figure 8*a* and *b*). The decay of the temperature cross-correlation in the wall-normal direction depends largely on the *TAR* and d. Larger *TAR* causes the correlation to remain larger near the interface, as the fluid temperature imprints on the surface more effectively. The maximum cross-correlation between the temperatures at the solid–fluid interface with $y = 0.4\delta$ decreases from 0.34 to 0.08 to 0.01 as *TAR* decreases from 1 to 0.1 to 0.01. The height of the solid domain has a similar effect on the correlation decay due to its correlation with heat penetration depth. With increasing d from 0.1 to 1 to 10, the maximum cross-correlation between the solid–fluid interfacial temperature with the temperature at $y = 0.4\delta$ increases from 0.11 to 0.34 to 0.46.

6. Conclusions

We expanded on work by Tiselj *et al.* (2001) on the effect of solid conduction on the heat transport mechanism without convective instability and work by Iida & Kasagi (1997) on the effect of convective instability on heat transport in channel flow. In the present study we have included both the effects of convective instability and solid conduction to examine the behaviour and effects of solid–fluid interfacial temperature variations.

The degree of convective instability affects the coherent structures. Streaks of low- and high-momentum fluid are observed in neutral channel flow. On the other end of the spectrum, in purely convective flow, plumes and downdrafts are the major flow features that cause stronger ejection and sweep events and stronger horizontally converging and diverging flow patterns. The turbulent structures are long and streaky in neutral channel flow compared with the cellular-like structure in purely convective flow. In-between these two extremes for convectively unstable flow, both buoyancy and shear are important and the plumes (downdrafts) tend to align one after another along the streamwise direction, and cause streamwise roll vortices in the bulk region of the channel flow. With the increase of convective instability, the ejection events become stronger compared to the sweep events. The imbalance between them can be successfully estimated by the third-order moments of the joint p.d.f.s (Raupach 1981; Katul *et al.* 2006*a*). The applicability of this observation for different Re_τ is not clear from the present study. For example, for larger Re_τ, scale separation may cause the higher order moments to have a more pronounced effect on the ejection and sweep events.

Despite the difference in the Re_τ and Ri_τ between the simulations ($Re_\tau = 180$–190 and $-Ri_\tau = 0.02$–4) and atmospheric observations ($Re_\tau \approx 10^7$, and $-Ri_\tau \approx 10^2$–10^3), mean and r.m.s. profiles of velocity and temperature for the convective atmospheric boundary layer are recovered. In a convective atmospheric boundary layer, the fluid temperature timeseries show ramp or sawtooth-like patterns, consisting of (i) constant temperature during the sweep event, (ii) slow increase in the transition from sweep to ejection and (iii) a sharp decrease during the ejection event (Taylor 1958; Kaimal & Businger 1970; Gao *et al.* 1989). The mechanism behind the temperature ramp pattern can be further explained by the surface renewal theory (Corino & Brodkey 1969; Brutsaert 1975; Paw U *et al.* 1995). In a convectively unstable environment as cold fluid descends during a sweep event, the temperature difference compared with the warmer background increases, and its downward velocity also decreases due to close proximity of the wall. As the fluid parcel remains near the warm wall, heat transfer from the wall to the fluid initially peaks, but then decreases due to heating of the fluid; eventually this leads to warming of the wall. With sufficient buoyancy the warm fluid ascends in an ejection, resulting in large heat transport from the wall to the fluid and decreasing wall temperature. Thus, the interface appears to be warm during the ejection and cold during the sweep. Similar to the atmospheric observation (Garai & Kleissl 2013; Garai *et al.* 2013) warm and cold structures at the solid–fluid interface are observed in the current DNS. Numerical simulations of the atmospheric boundary layer using large eddy simulation with appropriate analogues of Re_τ and Ri_τ will be considered in the future.

In the present DNS study, coupling the solid conduction to the fluid affects only the fluid temperature in the viscous or conduction sublayer as the fluid has $Pr = 1$. Thus, while the upper boundary condition is neither realistic for atmospheric boundary layers nor considers solid–fluid coupling as the bottom boundary condition, our conclusions pertaining to the effect of solid–fluid coupling are not affected by the dissimilarity of

the top and bottom boundary conditions. The fluid temperature fluctuations influence the interfacial temperature more effectively for smaller thermal inertia solids (larger *TAR*) with larger thickness. The heat transport mechanism behaves as isothermal with high surface heat flux variation for $TAR \to 0$, and as isoflux with high interfacial temperature variation for $TAR \to \infty$ by altering the thermal diffusion and thermal dissipation in the conduction sublayer, consistent with the findings of Tiselj *et al.* (2001). As only the larger-scale structures imprint on the surface, the influence of the solid–fluid coupling may be stronger in flows with larger friction Reynolds and Richardson numbers (for atmospheric convective boundary-layer flows $Re_\tau \approx 10^7$ and $-Ri_\tau \approx 10^2$–10^3). In the current simulations, the increase in the fluid temperature fluctuations in the conduction layer, depending on *TAR* and solid thickness, *d*, does not influence the turbulent structures, as the buoyant production vanishes in this region. Thus, the fluid temperature p.d.f. becomes Gaussian in the conduction sublayer, whereas in the outer layer the temperature distribution is positively skewed.

Although solid thermal properties and thickness do not influence turbulent structures, at least for present DNS cases, they strongly influence the solid–fluid interfacial temperatures. The accurate estimation of solid–fluid interfacial temperature is advantageous in environmental and engineering problems, such as irrigation management (Kleissl, Hong & Hendrickx 2009) and turbine blades in turbomachines (Duchaine *et al.* 2009), etc.

Acknowledgements

We are grateful to (i) NASA for funding through a New Investigator Program award, (ii) the NCAR-Wyoming Supercomputer Center (funded by the National Science Foundation and the State of Wyoming) which is supported by National Center for Atmospheric Research's (NCAR) Computational and Information System Laboratory and (iii) San Diego Supercomputer Center, Extreme Science and Engineering Discovery Environment (XSEDE) program, which is supported by National Science Foundation grant number OCI-1053575 for providing computing resources.

REFERENCES

AHLERS, G., GROSSMANN, S. & LOHSE, D. 2009 Heat transfer and large scale dynamic in turbulent Rayleigh–Bénard convection. *Rev. Mod. Phys.* **81**, 503–537.

ANTONIA, R. A., ABE, H. & KAWAMURA, H. 2009 Analogy between velocity and scalar fields in a turbulent channel flow. *J. Fluid Mech.* **628**, 241–268.

ARMENIO, V. & SARKAR, S. 2002 An investigation of stably stratified turbulent channel flow using large-eddy simulation. *J. Fluid Mech.* **459**, 1–42.

BALICK, L. K., JEFFERY, C. A. & HENDERSON, B. 2003 Turbulence induced spatial variation of surface temperature in high resolution thermal IR satellite imagery. *Proc. SPIE* **4879**, 221–230.

BALLARD, J. R., SMITH, J. A. & KOENIG, G. G. 2004 Toward a high temporal frequency grass canopy thermal IR model for background signatures. *Proc. SPIE* **5431**, 251–259.

DE BRUIN, H. A. R., KOHSIEK, W. & VAN DEN HURK, J. J. M. 1993 A verification of some methods to determine the fluxes of momentum, sensible heat, and water vapour using standard deviation and structure parameter of scalar meteorological quantities. *Boundary-Layer Meteorol.* **63**, 231–257.

BRUTSAERT, W. 1975 A theory for local evapotranspiration (or heat transfer) from rough and smooth surfaces at ground level. *Water Resour. Res.* **11**, 543–550.

CARSLAW, H. S. & JAEGER, J. C. 1959 *Conduction of Heat in Solids*. Oxford University Press.

CHRISTEN, A. & VOOGT, J. A. 2009 Linking atmospheric turbulence and surface temperature fluctuations in a street canyon. *The 7th International Conference on Urban Climate Paper A3-6*. The International Association for Urban Climate.

CHRISTEN, A. & VOOGT, J. A. 2010 Inferring turbulent exchange process in an urban street canyon from high–frequency thermography. *The 9th Symposium on the Urban Environment*, Paper J3A.3. American Meteorological Society, MA, USA.

CHU, C. R., PARLANGE, M. B., KATUL, G. G. & ALBERTSON, J. D. 1996 Probability density functions of turbulent velocity and temperature in the atmospheric surface layer. *Water Resour. Res.* **32**, 1681–1688.

COHN, S. A., MAYOR, S. D., GRUND, C. J., WECKWERTH, T. M. & SNEFF, C. 1998 The lidars in flat terrain (LIFT) experiment. *Bull. Am. Meteorol. Soc.* **79**, 1329–1343.

CORINO, E. R. & BRODKEY, R. S. 1969 A visual investigation of the wall region in turbulent flow. *J. Fluid Mech.* **37**, 1–30.

DERKSEN, D. S. 1974 Thermal infrared pictures and mapping of microclimate. *Neth. J. Agric. Sci.* **22**, 119–132.

DROBINSKI, P., BROWN, R. A., FLAMANT, P. H. & PELON, J. 1998 Evidence of organized large eddies by ground based Doppler lidar, sonic anemometer and sodar. *Boundary-Layer Meteorol.* **88**, 343–361.

DUCHAINE, D., CORPRON, A., PONS, L., MOUREAU, V., NICOUD, F. & POINSOT, T. 2009 Development and assessment of a coupled strategy for conjugate heat transfer with large eddy simulation: application to a cooled turbine blade. *Intl J. Heat Fluid Flow* **30**, 1129–1141.

GAO, W., SHAW, R. H. & PAW U, K. T. 1989 Observation of organized structure in turbulent flow within and above a forest canopy. *Boundary-Layer Meteorol.* **47**, 349–377.

GARAI, A. & KLEISSL, J. 2011 Air and surface temperature coupling in the convective atmospheric boundary layer. *J. Atmos. Sci.* **68**, 2945–2954.

GARAI, A. & KLEISSL, J. 2013 Interaction between coherent structures and surface temperature and its effect on ground heat flux in an unstably stratified boundary layer. *J. Turbul.* **14** (8), 1–23.

GARAI, A., PARDYJAK, E., STEENVELD, G. J. & KLEISSL, J. 2013 Surface temperature and surface layer turbulence in a convective boundary layer. *Boundary-Layer Meteorol.* **148**, 51–72.

GURKA, R., LIBERZON, A. & HETSRONI, G. 2004 Detecting coherent patterns in a flume by using PIV and IR imaging technique. *Exp. Fluids* **37**, 230–236.

HETSRONI, G., KOWALEWSKI, T. A., HU, B. & MOSYAK, A. 2001 Tracking of coherent thermal structures on a heated wall by means of infrared thermography. *Exp. Fluids* **30**, 286–294.

HETSRONI, G. & ROZENBLIT, R. 1994 Heat transfer to a liquid–solid mixture in a flume. *Intl J. Multiphase Flow* **20**, 671–689.

HÖGSTRÖM, U. L. F. 1988 Non-dimensional wind and temperature profiles in the atmospheric surface layer: a re-evaluation. *Boundary-Layer Meteorol.* **42**, 55–78.

HUNT, J. C. R., VRIELING, A. J., NIEUWSTADT, F. T. M. & FERNANDO, H. J. S. 2003 The influence of the thermal diffusivity of the lower boundary on eddy motion in convection. *J. Fluid Mech.* **491**, 183–205.

IIDA, O. & KASAGI, N. 1997 Direct numerical simulation of unstably stratified turbulent channel flow. *Trans. ASME J. Heat Transfer* **119**, 53–61.

JIMÉNEZ, J. 2012 Cascade in wall-bounded turbulence. *Annu. Rev. Fluid Mech.* **44**, 27–45.

JOHANSSON, A. V. & WIKSTRÖM, P. M. 1999 DNS and modelling of passive scalar transport in turbulent channel flow with a focus on scalar dissipation rate modelling. *Flow Turbul. Combust.* **63**, 223–245.

KADER, B. A. 1981 Temperature and concentration profiles in fully turbulent boundary layers. *Intl J. Heat Mass Transfer* **24**, 1541–1544.

KAIMAL, J. C. & BUSINGER, J. A. 1970 Case studies of a convective plume and a dust devil. *J. Appl. Meteorol.* **9**, 612–620.

KAIMAL, J. C., WYNGAARD, J. C., HAUGEN, D. A., COTE, O. R. & IZUMI, Y. 1976 Turbulence structure in the convective boundary layer. *J. Atmos. Sci.* **33**, 2152–2169.

KATUL, G. G., POGGI, D., CAVA, D. & FINNIGAN, J. J. 2006*a* The relative importance of ejections and sweeps to momentum transfer in the atmospheric boundary layer. *Boundary-Layer Meteorol.* **120**, 367–375.

KATUL, G. G., PORPORATO, A., CAVA, D. & SIQUERIA, M. B. 2006*b* An analysis of intermittency, scaling, and surface renewal in atmospheric surface layer turbulence. *Physica D* **215**, 117–126.

KATUL, G. G., SCHIELDGE, J., HSIEH, C. I. & VIDAKOVIC, B. 1998 Skin temperature perturbations induced by surface layer turbulence above a grass surface. *Water Resour. Res.* **3**, 1265–1274.

KIM, J., MOIN, P. & MOSER, R. 1987 Turbulence statistics in fully developed channel flow at low Reynolds number. *J. Fluid Mech.* **177**, 133–136.

KLEISSL, J., HONG, S. H. & HENDRICKX, J. M. H. 2009 New Mexico scintillometer network in support of remote sensing and hydrologic and meteorological models. *Bull. Am. Meteorol. Soc.* **90**, 207–218.

LEMONE, M. A. 1973 The structure and dynamic of horizontal roll vortices in the planetary boundary layer. *J. Atmos. Sci.* **30**, 1077–1091.

LENSCHOW, D. H. & BOBA STANKOV, B. 1986 Length scales in the convective boundary layer. *J. Atmos. Sci.* **43**, 1198–1209.

LOTHON, M., LENSCHOW, D. H. & MAYOR, S. D. 2006 Coherence and scale of vertical velocity in the convective boundary layer from a Doppler lidar. *Boundary-Layer Meteorol.* **121**, 521–536.

MONIN, A. S. & OBUKHOV, A. M. 1954 Basic laws of turbulent mixing in the surface layer of the atmosphere. *Tr. Akkad. Nauk SSSR Geophiz. Inst.* **24**, 163–187.

MORINISHI, Y., TAMANO, S. & NAKAMURA, E. 2007 New scaling of turbulence statistics for incompressible thermal channel flow with different total heat flux gradients. *Intl J. Heat Mass Transfer* **50**, 1781–1789.

MOSER, R. D., KIM, J. & MANSOUR, N. N. 1999 Direct numerical simulation of turbulent channel flow up to $Re_\tau = 590$. *Phys. Fluids* **11**, 943–945.

PAULSON, C. A. 1970 The mathematical representation of wind speed and temperature profiles in the unstable atmospheric surface layer. *J. Appl. Meteorol.* **9**, 857–861.

PAW U, K. T., QIU, J., SU, H.-B., WATANABE, T. & BRUNET, Y. 1995 Surface renewal analysis: a new method to obtain scalar fluxes. *Agric. Forest Meteorol.* **77**, 119–137.

PIERCE, B., MOIN, P. & SAYADI, T. 2013 Application of vortex identification schemes to direct numerical simulation data of a transitional boundary layer. *Phys. Fluids* **25**, 015102.

POPE, S. B. 2000 *Turbulent Flows*. pp. 1–771. Cambridge University Press.

RAASCH, S. & ETLING, D. 1991 Numerical simulation of rotating turbulent thermal convection. *Beitr. Phys. Atmos.* **64**, 185–199.

RAUPACH, M. R. 1981 Conditional statistics of Reynolds stress in rough-wall and smoothwall turbulent boundary layers. *J. Fluid Mech.* **108**, 363–382.

RENNO, N. O., ABREU, V. J., KOCH, J., SMITH, P. H., HARTOGENSIS, O. K., DE BRUIN, H. A. R., BUROSE, D., DELORY, G. T., FARRELL, W. M., WATTS, C. J., GARATUZA, J., PARKER, M. & CARSWELL, A. 2004 MATADOR 2002: a pilot experiment on convective plumes and dust devils. *J. Geophys. Res.* **109**, E07001.

SCHOLS, J. L. J. 1984 The detection and measurement of turbulent structures in the atmospheric surface layer. *Boundary-Layer Meteorol.* **29**, 39–58.

SCHOLS, J. L. J., JANSEN, A. E. & KROM, J. G. 1985 Characteristics of turbulent structures in the unstable atmospheric surface layer. *Boundary-Layer Meteorol.* **33**, 173–196.

SHISHKINA, O., STEVENS, R. J. A. M., GROSSMANN, S. & LOHSE, D. 2010 Boundary layer structure in turbulent covection and its consequences for the required numerical resolution. *New J. Phys.* **12**, 075022.

TAYLOR, R. J. 1958 Thermal structures in the lowest layers of the atmosphere. *Austral. J. Phys.* **11**, 168–176.

TISELJ, I., BERGANT, R., MAVK, M., BAJSIĆ, I. & HETSRONI, G. 2001 DNS of turbulent heat transfer in channel flow with heat conduction in the solid wall. *Trans. ASME J. Heat Transfer* **123**, 849–857.

VERZICCO, R. & SREENIVASAN, K. R. 2008 A comparison of turbulent thermal convection between conditions of constant temperature and constant heat flux. *J. Fluid Mech.* **595**, 203–219.

VOGT, R. 2008 Visualisation of turbulent exchange using thermal camera. *18th Symposium on Boundary Layer and Turbulence*, Paper 8B.1. American Meteorological Society, MA, USA.

WANG, X., CASTILLO, L. & ARAYA, G. 2008 Temperature scalings and profiles in forced convection turbulent boundary layers. *Trans. ASME J. Heat Transfer* **130**, 021701.

WARHAFT, Z. 2000 Passive scalars in turbulent flows. *Annu. Rev. Fluid Mech.* **32**, 203–240.

WICKER, L. J. & SKAMAROCK, W. C. 2002 Time-splitting methods for elastic models using forward time schemes. *Mon. Weath. Rev.* **130**, 2088–2097.

WILCZAK, J. M. & BUSINGER, J. A. 1983 Thermally indirect motions in the convective atmospheric boundary layer. *J. Atmos. Sci.* **40**, 343–358.

WILCZAK, J. M. & TILLMAN, J. E. 1980 The three-dimensional structure of convection in the atmospheric boundary layer. *J. Atmos. Sci.* **37**, 2424–2443.

WILLIAMSON, J. H. 1980 Low storage Runge–Kutta schemes. *J. Comput. Phys.* **35**, 48–56.

WYNGAARD, J. C., COTÉ, O. R. & IZUMI, Y. 1971 Local free convection, similarity and the budgets of shear stress and heat flux. *J. Atmos. Sci.* **28**, 1171–1182.

YOUNG, G. S. 1988*a* Turbulence strucutre of the convective boundary layer. Part I: variability of normalized turbulence statistics. *J. Atmos. Sci.* **45**, 712–719.

YOUNG, G. S. 1988*b* Turbulence strucutre of the convective boundary layer. Part II: phoenix 78 aircraft observations of thermals and their environment. *J. Atmos. Sci.* **45**, 727–735.

ZHOU, J., ADRIAN, R. J., BALACHANDAR, S. & KENDALL, T. M. 1999 Mechanism for generating coherent packets of hairpin vortices in channel flow. *J. Fluid Mech.* **387**, 353–396.